

Liquefaction mapping in finite element simulations

Kirk C. Ellisonⁱ, S.M. ASCE and José E. Andrade^{†ii}, A.M. ASCE

Abstract

Recent criteria have been developed to describe the onset of static liquefaction in constitutive models. This paper expands the theory to a finite element framework in order to predict potentially unstable regions in granular soils at the engineering scale. Example simulations are presented for two plane strain tests and a submarine slope to demonstrate the applicability of a proposed liquefaction criterion to boundary value problems. In addition, loading rate and mesh size effects on the liquefaction prediction are examined. The methodology presented herein shows promise as a means of predicting soil liquefaction based on solid mechanical theory rather than empiricism.

ⁱDepartment of Civil and Environmental Engineering, Northwestern University

[†]Corresponding author. E-mail: j-andrade@northwestern.edu (J. E. Andrade).

ⁱⁱDepartment of Civil and Environmental Engineering, Northwestern University

Introduction

The phenomenon of liquefaction occurs in saturated cohesionless soils when the rate of loading is so rapid that positive excess pore pressures develop before the water can drain away. As the pressures build up, the effective stress and shear strength may decrease to zero, causing the soil to behave like a liquid. While liquefaction is usually associated with earthquakes, the same phenomenon has been shown to occur under static loading conditions, causing serious damage to infrastructure from landslides, bearing capacity failures and the flotation of buried structures [Kramer, 1996; Lade, 1992].

Liquefaction is not synonymous with conventional definitions for failure. In triaxial tests, failure is typically defined by one of two criteria: (1) maximum principal stress difference, $(\sigma_1 - \sigma_3)_{\max}$; or (2) maximum effective principal stress ratio, $(\sigma'_1/\sigma'_3)_{\max}$ [Borja, 2006; Lade, 1992]. These two criteria are fulfilled simultaneously when pore pressures are allowed to dissipate during drained tests; however, the correct definition for failure is less clear for undrained conditions. In particular, loose sands may experience an increase in pore pressure that causes the maximum stress difference to be reached before the maximum effective stress ratio. Lade [1992] proposes that the true failure line corresponds to the maximum effective stress ratio, but that a shallower 'instability line' can be described that extends from the origin through the point of maximum stress difference on a plot of mean normal effective stress, $p' = (\sigma'_1 + 2\sigma'_3)/3$, versus principal stress difference, $q = \sigma_1 - \sigma_3$. Instabilities such as liquefaction can occur when the effective stress ratio is greater than the slope of the instability line, but less than the slope of the failure line. However, the precise conditions that result in the onset of such instabilities have proven more difficult to determine.

Recently, mathematical conditions have been proposed to signal the onset of static liquefaction in constitutive models [Andrade, 2009; Borja, 2006]. Borja [2006] derived a general liquefaction criterion for soils based on isotropic elastoplasticity through the formulation of a liquefaction matrix, \mathbf{L} . Shortly afterward, Andrade [2009] derived a liquefaction criterion for slightly simplified assumptions based on the value of a critical hardening modulus, H_{crit} . This is a convenient way to define liquefaction because the hardening modulus, H , is a key

component in most constitutive models that describes the evolution of the elastic region with respect to plastic strains. The onset of static liquefaction then occurs simply when $H = H_{\text{crit}}$, which is analagous to the way that the onset of localization is described by Rudnicki and Rice [1975]. Additionally, and perhaps more importantly, this criterion underscores the dependence of the onset of liquefaction flow on the state of the sand. This is in sharp contrast with the state of the practice, where the onset of instability is determined by the instability line as a sufficient condition. The instability line of Lade [1992] is a necessary condition for flow liquefaction [Andrade, 2009].

Andrade [2009] unifies the above two criteria with previously developed conditions for “loss of controllability” in Nova [1994] and Pradel and Lade [1990] by showing that they are all equivalent for the case of undrained triaxial compression. In addition, Andrade [2009] verifies the critical hardening modulus criterion by replicating Lade’s instability line for an infinitesimal homogeneous soil element [Lade, 1992]. Now that the condition leading to liquefaction in constitutive models has been identified, the time has come to perform large scale simulations. This follow-up paper to Andrade [2009] examines the propagation of static liquefaction in boundary value problems in order to demonstrate the usefulness and applicability of liquefaction criteria to real-world situations.

The following section will discuss the Borja [2006] and Andrade [2009] liquefaction criteria in more detail. Section 3 will then briefly describe a constitutive model for sands based on Critical State Soil Mechanics (CSSM). In Section 4, the liquefaction criteria and constitutive model presented in Sections 2 and 3 will be incorporated into a finite element framework to map the propagation of static liquefaction throughout several monotonic loading sequences.

As for notations and symbols used in this paper, bold-faced letters denote tensors and vectors, italic subscripts indicate dimensional components (e.g. $\mathbf{d} = d_i = [d_1 \ d_2 \ d_3]$) and repeated indices are summed. In addition, the symbol ‘:’ denotes an inner product of two second-order tensors (e.g. $\mathbf{c} : \mathbf{d} = c_{ij}d_{ij}$), or a double contraction of adjacent indices of tensors of rank two and higher (e.g. $\mathbf{C} : \boldsymbol{\epsilon}^e = C_{ijkl}\epsilon_{kl}^e$). Mechanics convention is used throughout the paper where tension is positive and compression is negative, unless otherwise stated.

Formulation of the liquefaction criterion

The derivations of two proposed mathematical conditions for the onset of liquefaction are briefly examined here. The interested reader is referred to Borja [2006] and Andrade [2009] for complete derivations of the following criteria.

Borja [2006] derives a general liquefaction criterion from thermodynamic principles based on isotropic elastoplasticity and bifurcation theory (the theory that instabilities develop when a loss of equilibrium results in multiple feasible solutions) [Hill, 1958]. Assuming that the interstitial fluid is incompressible and that the bulk modulus of the soil, K , is negligible compared with the bulk modulus of the solid constituent, K_s (i.e. $K \ll K_s$), a simplified series of homogeneous equations can be developed as follows

$$\underbrace{\begin{bmatrix} c_{11}^{\text{ep}} & c_{12}^{\text{ep}} & c_{13}^{\text{ep}} & -1 \\ c_{21}^{\text{ep}} & c_{22}^{\text{ep}} & c_{23}^{\text{ep}} & -1 \\ c_{31}^{\text{ep}} & c_{32}^{\text{ep}} & c_{33}^{\text{ep}} & -1 \\ -1 & -1 & -1 & 0 \end{bmatrix}}_{\mathbf{L}} \begin{Bmatrix} \llbracket \dot{\epsilon}_1 \rrbracket \\ \llbracket \dot{\epsilon}_2 \rrbracket \\ \llbracket \dot{\epsilon}_3 \rrbracket \\ \llbracket \dot{p} \rrbracket \end{Bmatrix} = \begin{Bmatrix} 0 \\ 0 \\ 0 \\ 0 \end{Bmatrix} \quad (1)$$

where c_{ij}^{ep} are the small strain constitutive moduli in principal directions, $\llbracket \dot{\epsilon}_j \rrbracket$ are the jumps in strain rates due to potentially duplicate solutions, $\llbracket \dot{p} \rrbracket$ is the jump in the rate of change of the pore fluid pressure, and \mathbf{L} is what Andrade [2009] later calls the liquefaction matrix. For a nontrivial solution to exist, the determinant of the liquefaction matrix must be equal to zero, thus liquefaction occurs when

$$\det \mathbf{L} = 0 \quad (2)$$

Andrade [2009] derives a comparable liquefaction criterion for the case of two-invariant plasticity under triaxial loading. Using the classical invariants

$$p' = \frac{1}{3} \text{tr } \boldsymbol{\sigma}'; \quad q = \sqrt{\frac{2}{3}} \|\boldsymbol{\xi}'\| \quad (3)$$

where $\boldsymbol{\sigma}'$ is the effective stress tensor and $\boldsymbol{\xi}'$ is the deviatoric part of the effective stress tensor, the yield surface and plastic potential equations can be expressed as $F = F(p', q, \pi_i)$ and $Q = Q(p', q, \bar{\pi}_i)$ with the variables π_i and $\bar{\pi}_i$ controlling the size of the surfaces described by F and Q , respectively. When Hill's instability criterion is combined with Terzaghi's effective stress equation (i.e., $\boldsymbol{\sigma}' = \boldsymbol{\sigma} + p\mathbf{1}$) and rewritten in the framework of elastoplasticity, it can take the form

$$[[\dot{\boldsymbol{\sigma}}]] : [[\dot{\boldsymbol{\epsilon}}]] = [[\dot{\boldsymbol{\epsilon}}]] : \mathbf{c}^{ep} : [[\dot{\boldsymbol{\epsilon}}]] - [[\dot{p}]]\mathbf{1} : [[\dot{\boldsymbol{\epsilon}}]] = 0 \quad (4)$$

where $[[\dot{\boldsymbol{\sigma}}]]$ is the jump in the rate of change of the total stress tensor, $\mathbf{1}$ is the identity matrix and \dot{p} is the rate of change of the pore pressure [Hill, 1958]. From equation (4) and the aforementioned assumptions of incompressible fluids and solids under triaxial loading conditions, one can derive the value for a critical hardening modulus [Andrade, 2009]

$$H_{\text{crit}} = -K \frac{\partial F}{\partial p'} \frac{\partial Q}{\partial p'} \quad (5)$$

Static liquefaction first occurs when $H = H_{\text{crit}}$ where the hardening modulus H is found by

$$H = -\frac{1}{\dot{\lambda}} \frac{\partial F}{\partial \pi_i} \dot{\pi}_i \quad (6)$$

for a two-invariant yield surface with $\dot{\lambda}$ as the plastic strain rate [Andrade and Borja, 2006] and $\dot{\pi}_i$ as the rate of change of the size variable π_i .

In Section 4, $H - H_{\text{crit}}$ will be plotted across each Gauss point for several finite element simulations. The critical hardening modulus criterion will be used to define static liquefaction and thus, liquefaction takes place when $H - H_{\text{crit}} \leq 0$.

Remark 1. It has been shown in Andrade [2009] that under triaxial conditions $\det \mathbf{L} = 0$ and $H - H_{\text{crit}} = 0$ are equivalent criteria for liquefaction instability.

Remark 2. It is illuminating to look at the liquefaction phenomenon from the point of view of loss of controllability as defined by Nova [1994]. In this context, we can think of a classical triaxial experiment conducted under undrained conditions. Under these conditions, one can

show that the above class of elastoplastic models boils down to

$$\begin{Bmatrix} \dot{\epsilon}_v \\ \dot{\epsilon}_s \end{Bmatrix} = \begin{bmatrix} 1/K + 1/H \partial_{p'} Q \partial_{p'} F & 1/H \partial_{p'} Q \partial_q F \\ 1/H \partial_q Q \partial_{p'} F & 1/(3\mu) + 1/H \partial_q Q \partial_q F \end{bmatrix} \begin{Bmatrix} \dot{p}' \\ \dot{q} \end{Bmatrix} \quad (7)$$

with μ as the elastic shear modulus, $\dot{\epsilon}_v := \dot{\epsilon}_a + 2\dot{\epsilon}_r$ as the volumetric invariant and $\dot{\epsilon}_s := 2/3|\dot{\epsilon}_a - \dot{\epsilon}_r|$ as the deviatoric invariant of the strain rate tensor. Also, $\dot{p}' = 1/3(\dot{\sigma}'_a + 2\dot{\sigma}'_r)$ and $\dot{q} = |\dot{\sigma}_a - \dot{\sigma}_r|$ under triaxial loading. Since liquefaction instability is associated with the peak of the $p' - q$ stress path in an undrained triaxial test, we require $\dot{q} = 0$. Furthermore, under undrained conditions, $\dot{\epsilon}_v = 0$, thus

$$\left(\frac{1}{K} + \frac{1}{H} \frac{\partial Q}{\partial p'} \frac{\partial F}{\partial p'} \right) \dot{p}' = 0 \quad (8)$$

and since $\dot{p}' \neq 0$, in general, the term inside the parentheses must vanish. It is worthwhile noting that this expression was also obtained by Pradel and Lade [1990] in the context of Hill's instability condition (see Hill [1958]). This critical term sheds some light into the mechanisms governing liquefaction instability. Let us consider the simplified case of associative plasticity, $F = Q$. In frictional materials, the term $\partial F / \partial p'$ is associated with the plastic volumetric strain rates, with the vanishing of such a term signifying zero volumetric plastic strain change or isochoric deformations. Elastic incompressibility would force liquefaction to occur at zero plastic volumetric strain rates. At the other extreme, large elastic compressibility would require large contractancy and/or a nearly perfectly plastic (though negative) hardening modulus. However, the elastic compressibility is usually finite (albeit small) and hence liquefaction occurs under compactive strains associated with softening. Once the material undergoes a so-called phase transformation point [Ishihara et al., 1975], transitioning from compaction to dilation, liquefaction cannot occur as the material must undergo hardening to accommodate phase transformations.

Formulation of the constitutive model

Even when using the above criteria, liquefaction predictions are only as accurate as the constitutive model used to make them and are a direct function of the state via the hardening modulus H . The simulations presented in Section 4 will use a model founded in CSSM [Schofield and Wroth, 1968]. In particular, it is an offspring of the ‘Nor-Sand’ model proposed by Jefferies [1993]. Its predictive capabilities have been verified under monotonic loading conditions in Andrade and Ellison [2008] and its complete formulation and numerical implementation in a finite element program are presented in Andrade and Borja [2006] and Borja and Andrade [2006]. This same constitutive model has already been used to predict the onset of localization in boundary value problems as well as the onset of liquefaction for an infinitesimal soil element [Andrade, 2009; Andrade and Borja, 2006; Andrade et al., 2007]. Some key features of the elastoplastic model are presented here.

The complete state of the soil is described by the classical invariants p' and q defined by Equation 3 as well as a state parameter, $\psi = v - v_c$, that measures the difference between the specific volume v and the specific volume at critical state v_c for the given pressure p' . The implicit assumption here is that a critical state line exists on a plot of $\ln p'$ versus v with a slope $\hat{\lambda}$ and a reference specific volume v_{c0} . It will be seen later on that ψ plays an important role in driving dilatant behavior in dense sands.

The elastic region exhibits hyperelasticity wherein the bulk and shear moduli are pressure-dependent [Houlsby, 1985]. For the following simulations, we have assumed that the deviatoric and volumetric responses are decoupled (i.e. the deviatoric response is not influenced by the volumetric response and vice versa); therefore the elastic shear modulus simplifies to a constant, $\mu = \mu_0$, and the bulk modulus is determined by $K = -p'/\hat{\kappa}$ where $\hat{\kappa}$ is the elastic compressibility constant.

The elastic region is enclosed by a yield surface based on p' , q and a third invariant

$$\frac{1}{\sqrt{6}} \cos 3\theta = \frac{\text{tr } \xi'^3}{\left(\sqrt{\text{tr } \xi'^2}\right)^3} \quad (9)$$

where θ is the Lode angle shown in Figure 1(a). The yield surface equation then takes the form

$$F(p', q, \theta, \pi_i) = \zeta(\theta)q + p'\eta(p', \pi_i) \quad (10)$$

where

$$\eta = \begin{cases} M[1 + \ln(\pi_i/p')] & \text{if } N = 0 \\ M/N[1 - (1 - N)(p'/\pi_i)^{N/(1-N)}] & \text{if } N > 0 \end{cases} \quad (11)$$

In the above equations, the constant geometric parameters M and N govern the shape of the yield surface in the meridian plane and π_i is the ‘image pressure’ that corresponds to the peak deviatoric stress as shown in Figure 1(b). Note that π_i is linearly proportional to the preconsolidation pressure, p_c ; thus, π_i can initially be found by the relationship between M , N , and p_c . While the yield surface for two-invariant models is usually characterized by a circle in the deviatoric plane, the variable $\zeta(\theta)$ controlled by the third invariant allows for a wider variety of convex shapes. For this model, it is defined as

$$\zeta(\theta) = \frac{(1 + \rho) + (1 - \rho) \cos 3\theta}{2\rho} \quad (12)$$

where ρ is a constant geometric parameter as shown in Figure 1(a).

The plastic potential is given by an equation parallel to the yield surface equation that takes the form

$$Q(p', q, \theta, \bar{\pi}_i) = \zeta(\theta)q + p'\bar{\eta}(p', \bar{\pi}_i) \quad (13)$$

where $\bar{\eta}$ is dependent on the plastic potential parameter \bar{N} and $\bar{\pi}_i$ is a free variable.

Isotropic hardening and softening of the yield surface is controlled by π_i with the hardening law, $\dot{\pi}_i = h(\pi_i^* - \pi_i)\dot{\epsilon}_s^p$, where $\dot{\pi}_i$ is the rate of change of the image pressure, h is a constant hardening parameter, π_i^* is a limiting image pressure, and $\dot{\epsilon}_s^p$ is the rate of change of plastic shear strain. The value of π_i^* is governed by the limiting plastic dilatancy, $D^* = (\dot{\epsilon}_v^p / \dot{\epsilon}_s^p)_{max}$ where $\dot{\epsilon}_v^p$ is the rate of change of plastic volumetric strain. Conveniently, Jefferies [1993] shows

from a number of laboratory test results that $D^* \approx 3.5\psi_i$ for sands, where $\psi_i = \psi + \hat{\lambda}\ln(\pi_i/p')$ denotes the distance between v and $v_{c,i}$, the specific volume on the critical state line that corresponds to π_i .

Finite element simulations

Three finite element simulations are presented herein that map the onset and propagation of static liquefaction throughout loading sequences using the critical hardening modulus criterion derived by Andrade [2009]. Two of these simulations represent variants of the simple plane strain test where the first case is sheared under compression and the second case is subjected to an increasing upward fluid flow gradient. The third simulation looks at a submarine slope that is subjected to an increasing vertical stress along the uphill surface. These predictions are compared against the well-established method proposed by Lade [1992] for the instability of submerged slopes. The boundary conditions and shearing mechanism are summarized in Table 1 and the material parameters and initial conditions are summarized in Table 2 for each test. Finally, the effects of loading rate and mesh coarseness on the liquefaction predictions are each examined for a set of simulations.

The simulations presented in this section use Q9P4 elements, indicating that the elements consist of two-dimensional quadrilaterals with nine displacement nodes and four pore pressure nodes. The finite element scheme combines stress/strain computations with pore pressure/flux effects via the classical implicit backward Euler algorithm in terms of displacement \mathbf{u} , pore pressure p and a time step Δt

$$\begin{Bmatrix} \mathbf{u} \\ p \end{Bmatrix}_{n+1} = \begin{Bmatrix} \mathbf{u} \\ p \end{Bmatrix}_n + \Delta t \begin{Bmatrix} \dot{\mathbf{u}} \\ \dot{p} \end{Bmatrix}_{n+1} \quad (14)$$

From the above equation and a system of nonlinear equations involving \mathbf{u} and p , one can derive a finite element scheme using Newton-Raphson iterations that accounts for fluid flow. The interested reader is referred to Andrade and Borja [2007] for the complete $\mathbf{u} - p$ formulation used for this ‘home-grown’ finite element software.

It should be noted that the value of H_{crit} is only approximated in the following simulations since the conditions of two-invariant plasticity and triaxial loading are not met. However, comparisons with the general criterion presented in Borja [2006] reveal that the instant and location of liquefaction predicted by the two criteria do not vary by more than a few short time steps for these cases.

Plane strain tests

The plane strain test simulations were performed on 5×10 cm samples (10×20 element meshes) with identical model parameters as shown in Table 2. In addition, each test was initially isotropically consolidated to a pressure of 100 kPa with a void ratio $e_0 = 1.0$ and a previous consolidation pressure $p_c = 110$ kPa before shearing.

Case 1: Undrained compression

The first case simulates a globally undrained compression test where the sample is sheared, after consolidation, by displacement of the top boundary at a constant nondimensional loading rate, $Z = 900$, where $Z = \dot{u}_y/k$ with \dot{u}_y as the downward rate of displacement of the top boundary and k as the hydraulic conductivity of the soil. It will be shown later in Section 4.3 that the local drainage behavior depends on the ratio Z rather than the individual parameters \dot{u}_y and k for unidirectional loading. Figure 2 presents the progression of liquefaction for this globally undrained simulation. Shortly after the load is applied, the entire specimen experiences plastic deformation as shown in Figure 2(g). The liquefaction criterion has little variation throughout the specimen at this stage, but one can already see that the specimen is closest to liquefying near the bottom due to gravity effects. Figure 2(h) captures the moment when liquefaction is first achieved. At this instant, the liquefaction criterion, $H - H_{\text{crit}}$, dips below zero at a Gauss point for the first time. Experimental data suggests that the onset of static liquefaction coincides with the moment of peak axial stress in undrained triaxial compression laboratory tests and, indeed, this is what we observe for the globally undrained plane strain simulation in Figure 2 as well [Doanh et al., 1997; Lade, 1992]. The post-

liquefaction behavior of the specimen trends toward a shear band as shown in Figure 2(i). Rapid relative compression in the shear band region results in the expulsion of water and elastic unloading elsewhere in the specimen.

In addition to the liquefaction criterion, Figure 2 also maps deviatoric strains and pore pressures throughout the loading sequence for comparison. The trends apparent in each set of plots are strikingly similar. Figures 2(a) through 2(c) show that higher pore pressures develop in the liquefaction-prone regions, and that this ultimately creates the fluid flow field denoted by the white arrows. Likewise, Figures 2(d) through 2(f) show that higher deviatoric strains develop in the same liquefaction-susceptible regions. Thus, all three measures of the state of the specimen are closely related.

Remark 3. The lower left corner of the sample is restrained by a ‘pin’ for stability considerations. Gravity effects (though small) make the sample want to expand more at the bottom than at the top. The lower left corner is restrained while the lower right corner is free to expand. This triggers small asymmetries, which propagate as the sample is further deformed. Hence the asymmetric responses reported in Figure 2.

Case 2: Increasing pore pressure gradient

The test specimen was subjected to a constant isotropic compressive pressure of 100 kPa throughout this simulation. During consolidation, the pore pressures along the top and bottom were fixed at zero to represent free-draining surfaces while the sides were modeled as no flow boundaries. After consolidation, the pore pressure along the bottom was increased at a constant rate while the pore pressure along the top was kept constant to introduce a pore pressure gradient. Since the nondimensional loading rate Z does not apply for this example, a hydraulic conductivity of 2.45×10^{-3} cm/s was specified. This scenario is not unlike that for which rising water levels on the upstream side of a dam result in greater pore pressure gradients on the downstream side. As with all of the simulations presented herein, the specimen response is time-dependent due to the effects of fluid flow. For this particular simulation, the pore pressure change was applied quite rapidly, at 0.95 kPa/s.

Liquefaction criterion plots for Case 2 are shown in Figure 3. For a pore pressure differential $\Delta p = 37$ kPa in Figure 3(a), the bottom of the sample has been disturbed sufficiently to yield a plastic response; however, the sample has not yet reached liquefaction. For $\Delta p = 55$ kPa in Figure 3(b), the gradient has perturbed a greater portion of the specimen than before and liquefaction is finally reached at the bottom corners. Figure 3(c) for $\Delta p = 95$ kPa shows how the liquefying region progresses upward as the gradient is increased beyond the first instant of liquefaction. At this step, the specimen has expanded slightly due to the vertical flow and the base has begun to displace outward due to the weight of the overlying soil. While neither a shear band nor a catastrophic failure resulted from this simulation, it is clear that the specimen is very unstable in Figures 3(b) and 3(c). Even more significant displacements would be expected during the liquefaction stage under non-isotropic loading conditions.

Case 3: Submarine slope

The final scenario considered a 10 meter high slope with a 30 degree incline, the top of which was submerged beneath 5 meters of water as shown in Figure 4. This simulation was meant to model the application of hydraulic fill above an underwater incline. The horizontal surfaces modeled above and below the slope extended for lengths of 20.0 and 18.7 meters, respectively, while the soil beneath the bottom of the slope extended for another 10 vertical meters. The bottom of the simulated area was fixed against vertical displacement and the sides were fixed against lateral displacement. In addition, the bottom and sides were modeled as no flow boundaries. The model parameters used for this simulation are given in Table 2. The simulation also assumes an initial void ratio $e_0 = 0.9$ and a hydraulic conductivity $k = 3.1 \times 10^{-3}$ cm/s. During the consolidation phase, the slope settled elastically under its own weight with pore pressures applied at the surface in correspondence with the weight of the overlying water. Once a steady state was achieved, preconsolidation pressures were assigned to the constitutive model to make each element approximately normally consolidated. Finally, an increasing uniform pressure was applied rapidly along a ten-meter span near the top of the slope until failure.

The pore pressures, deviatoric strains and liquefaction criterion values at the onset of flow failure are presented in Figure 5. Flow failure was known to be achieved because the simulated region could not resist any further stress increase along the top of the slope. This instant coincided with the first appearance of a liquefying region below the area of applied pressure. As expected, the liquefying region in Figure 5(c) corresponds with the areas of high pore pressure and high deviatoric strain in Figures 5(a) and 5(b). It is important to compare these predictions to established methods used in the field to analyze the stability of submerged slopes.

Therefore, this example provides a good opportunity to compare the new framework with an established method first presented by Lade [1992], which defines a separate parameter, ϕ'_I , as the effective instability friction angle. In Lade [1992], potentially unstable regions are identified for instances when Spencers slope stability method would indicate that the slope is generally stable (i.e. the slope has a factor of safety greater than unity). Utilizing the assumption that the factor of safety along a given slip surface is uniform, stress states may be found at points along numerous trial surfaces that can then be checked for potential instabilities in cohesionless materials (i.e., $\tau/\sigma' = \tan \phi'_I$, where τ is shear stress and σ' is the effective normal stress). Hence, in principle, given the effective instability friction angle, one can perform straightforward slope stability analyses to determine the stability of submerged slopes.

Figures 6(a) and 6(b) present the potentially unstable region predicted by the Lade [1992] method for the example described in this section assuming a critical pressure of 175 kPa/m is applied at the top of the slope. More than fifty slip surfaces were evaluated using the computer program SLOPE/W, but only five are shown here for ease of presentation. In general, there seems to be agreement between the methods as the onset of the instability in Figure 5(c) occurs at a point within or very near the region described in Figure 6(b). For this analysis, the effective (peak) friction angle $\phi' = 32$ degrees was calculated from the parameter $M=1.27$, and $\phi_I = 29$ degrees was estimated from a series of numerical simulations of undrained triaxial compression tests.

Remark 4. Even though the results of the proposed method are comparable to that of Lade [1992] there are two significant differences that must be pointed out. First, Lade [1992] method is a limit equilibrium analysis, and as such, the deformations ensuing from the liquefaction instabilities cannot be determined directly. Second, and perhaps equally important, Lade [1992] method is based on the concept of the instability line and hence requires the specification of the ‘parameter’ ϕ'_I . It has been shown in Andrade [2009] that liquefaction instability is not a material parameter, but rather a function of the sand state, as evidenced by the hardening modulus. For instance, denser sands could mobilize friction angles above ϕ'_I without undergoing flow liquefaction.

Discussion of loading rate effects

The rate of drainage in finite element simulations depends on the hydraulic conductivity k of the soil and an applied rate of displacement \dot{u}_y for vertically loaded samples. However, using the Buckingham- π theorem [Buckingham, 1914] and the partial differential equations implied by the laws of balance of mass and balance of linear momentum, one can derive a single nondimensional parameter $Z = \dot{u}_y/k$ that controls the rate of fluid flow during unidirectional loading. Thus, the predicted behavior for any simulation with a given Z will be the same, regardless of the individual values of the parameters \dot{u}_y and k .

Example simulations for a 5×10 cm specimen under plane strain compression are provided in Figure 7 assuming relatively homogeneous conditions in order to demonstrate the effect of the loading rate on liquefaction predictions. For this set of simulations, the specimen was isotropically consolidated to a pressure of 100 kPa, and sheared by displacement of the top boundary at a constant rate. Drainage was permitted only along the upper surface, where p was fixed at zero. The constitutive model parameters are identical to those used for the plane strain tests in Section 4.1. The various curves in Figure 7 represent simulations having different loading rates ranging from locally drained, $Z \Rightarrow 0$ (lower limit), to locally undrained, $Z \Rightarrow \infty$ (upper limit). As one would expect, higher Z -values correspond with higher stresses early in the loading sequence as the load is initially taken up by excess pore pressures that

dissipate more slowly. Likewise, as Z decreases, the onset of liquefaction occurs at higher strains, up to a critical loading rate beyond which the specimen does not liquefy at all. For the examples in the figure, liquefaction takes place in the simulations where $Z \geq 500$ (i.e., the loading rate must be at least two orders of magnitude higher than the hydraulic conductivity for liquefaction to occur in this context).

Mesh sensitivity

A sensitivity analysis was conducted to determine the effects of mesh coarseness on the simulation predictions. Undrained plane strain compression tests were simulated using meshes of 50, 200 and 800 elements to represent a 5×10 cm specimen as in Case 1. The result of this analysis is summarized in Figure 8. The behavior of each simulation is identical up to around 0.4 percent axial strain when the 800 element mesh reached its peak axial stress. Shortly thereafter, the 200 and 50 element meshes reached their peaks at 0.45 and 0.5 percent axial strain, respectively. The point of liquefaction for each simulation approximately corresponded with the peak stress; thus, the prediction for the onset of liquefaction does exhibit some mesh dependence. In addition, the suddenness of strength loss appears to be proportional to the number of elements in the mesh.

Conclusions

For the first time, recently developed liquefaction criteria have been employed to map the progression of static liquefaction in large-scale boundary value problems. The three sample cases examined above demonstrate that the onset and location of liquefaction-induced instabilities can be identified by realistic numerical models. The two plane strain laboratory test simulations yielded realistic results that show loss of stability for an entire specimen approximately coincides with the first instant of liquefaction at a point. The case of instability in a submarine slope demonstrates the usefulness of the liquefaction criteria for a realistic engineering problem. This proof-of-concept opens the door for more advanced study of the mechanism of liquefaction than previously possible. In addition, this paper has shown that liquefaction risk

assessments of slope and bearing capacity failures can be performed based on solid mechanical theory rather than empiricism. In the near future, predictive numerical models using the liquefaction criteria employed here may provide a practical option for evaluating site-specific liquefaction susceptibility.

Acknowledgments

K.C.E. would like to acknowledge the partial support of his M.S. studies at Northwestern via a Walter P. Murphy Graduate Fellowship. Also, the authors are grateful to the anonymous reviewers for their insightful comments.

Accepted Manuscript
Not Copyedited

References

- J. E. Andrade. A predictive model for static liquefaction. *Géotechnique*. In press, 2009.
- J. E. Andrade and R. I. Borja. Capturing strain localization in dense sands with random density. *International Journal for Numerical Methods in Engineering*, 67:1531–1564, 2006.
- J. E. Andrade and R. I. Borja. Modeling deformation banding in dense and loose fluid-saturated sands. *Finite Elements in Analysis and Design*, 43:361–383, 2007.
- J. E. Andrade and K. C. Ellison. Evaluation of a predictive constitutive model for sands. *Journal of Geotechnical and Geoenvironmental Engineering*, 134:1825–1828, 2008.
- J. E. Andrade, J. W. Baker, and K. C. Ellison. Random porosity fields and their influence on the stability of granular media. *International Journal for Numerical and Analytical Methods in Geomechanics*, 32:1147–1172, 2007.
- R. I. Borja. Condition for liquefaction instability in fluid-saturated granular soils. *Acta Geotechnica*, 1:211–224, 2006.
- R. I. Borja and J. E. Andrade. Critical state plasticity, Part VI: Meso-scale finite element simulation of strain localization in discrete granular materials. *Computer Methods in Applied Mechanics and Engineering*, 195:5115–5140, 2006.
- E. Buckingham. On physically similar systems; illustrations of the use of dimensional equations. *Physical Review*, 4:345–376, 1914.
- T. Doanh, E. Ibraim, and R. Mاتيotti. Undrained instability of very loose hostun sand in triaxial compression and extension. Part 1: experimental observations. *Mechanics of Cohesive-Frictional Materials*, 2:47–70, 1997.
- R. Hill. A general theory of uniqueness and stability in elastic-plastic solids. *Journal of the Mechanics and Physics of Solids*, 6:236–249, 1958.
- G. T. Houlsby. The use of a variable shear modulus in elasto-plastic models for clays. *Computers and Geotechnics*, 1:3–13, 1985.

- K. Ishihara, F. Tatsuoka, and S. Yasuda. Undrained deformation and liquefaction of sand under cyclic stresses. *Soils and Foundations*, 15:29–44, 1975.
- M. G. Jefferies. Nor-Sand: a simple critical state model for sand. *Géotechnique*, 43:91–103, 1993.
- S. L. Kramer. *Geotechnical Earthquake Engineering*. Prentice-Hall, New Jersey, 1996.
- P. V. Lade. Static instability and liquefaction of loose fine sandy slopes. *Journal of Geotechnical Engineering, ASCE*, 118:51–71, 1992.
- R. Nova. Controllability of the incremental response of soil specimens subjected to arbitrary loading programmes. *Journal of the Mechanical Behavior of Materials*, 5:193–201, 1994.
- D. Pradel and P. V. Lade. Instability and plastic flow of soils. I: analytical investigation. *Journal of Engineering Mechanics*, 116:2551–2566, 1990.
- J. W. Rudnicki and J. R. Rice. Conditions for localization of deformation in pressure-sensitive dilatant materials. *Journal of the Mechanics and Physics of Solids*, 23:371–394, 1975.
- A. Schofield and P. Wroth. *Critical State Soil Mechanics*. McGraw-Hill, New York, 1968.

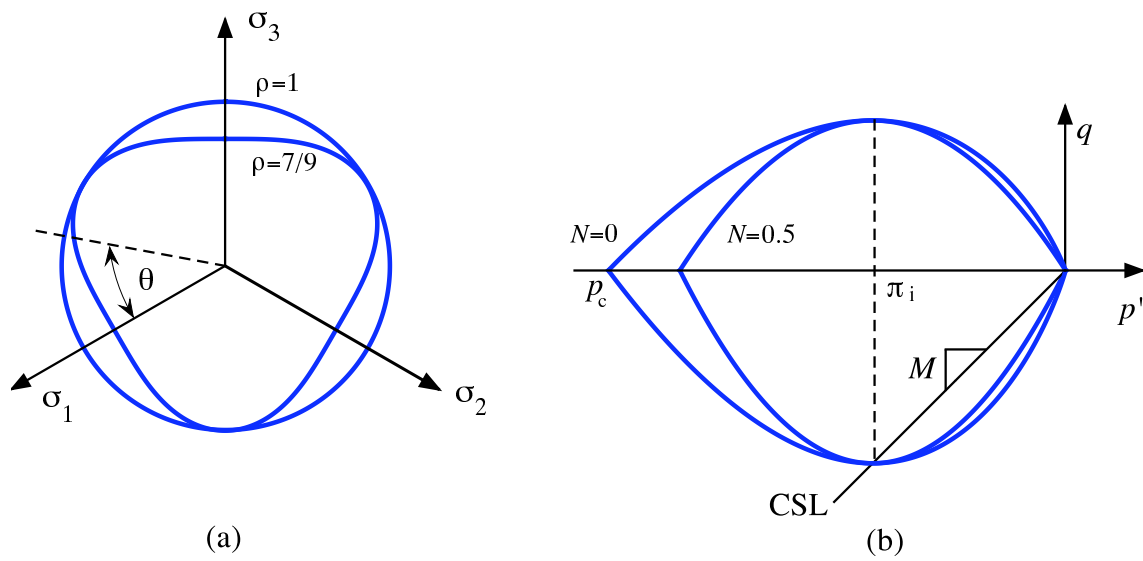
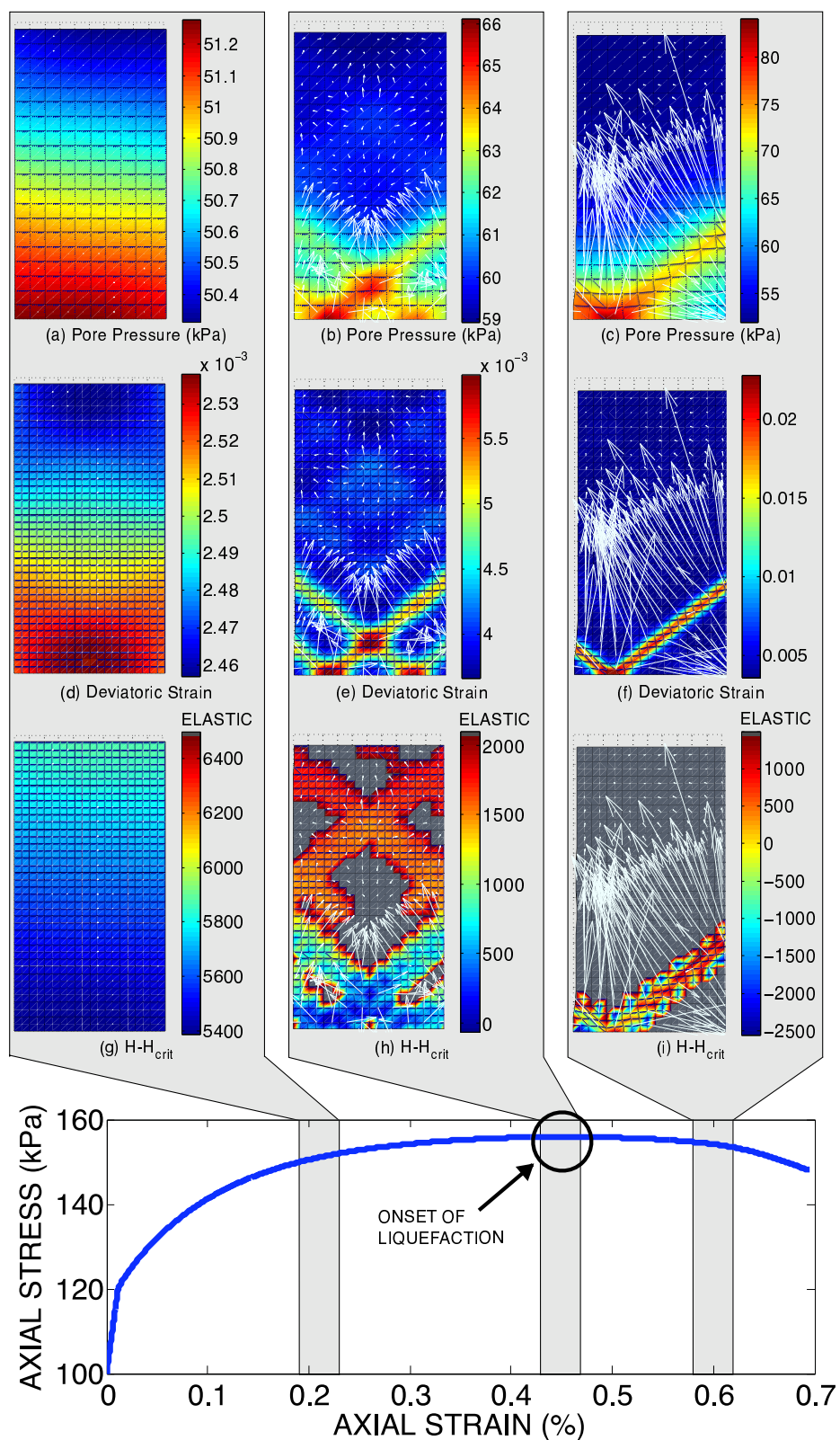


Figure 1: Three invariant yield surface on (a) deviatoric plane at different values of ρ and (b) meridian plane at different values of N (from Andrade et. al. [2007]).

Accepted Manuscript
 Not Copyedited



Accepted Manuscript
Not Copyedited

Figure 2: Mapping of pore pressure, deviatoric strain and $H - H_{crit}$ criterion for Case 1: undrained plane strain compression. (Note: Deformations are magnified $\times 10$).

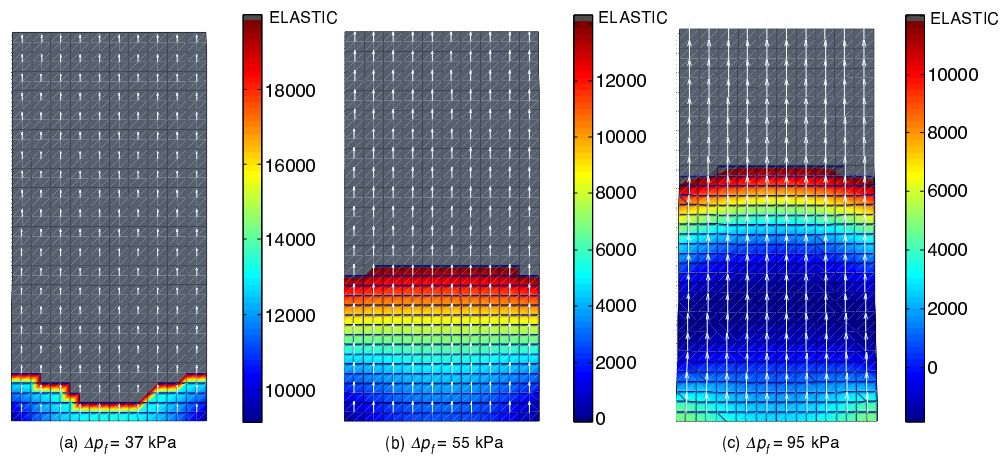


Figure 3: Liquefaction mapping of $H - H_{crit}$ for Case 2: Increasing pore pressure gradient. (Note: Deformations are magnified $\times 10$).

Accepted Manuscript
Not Copyedited

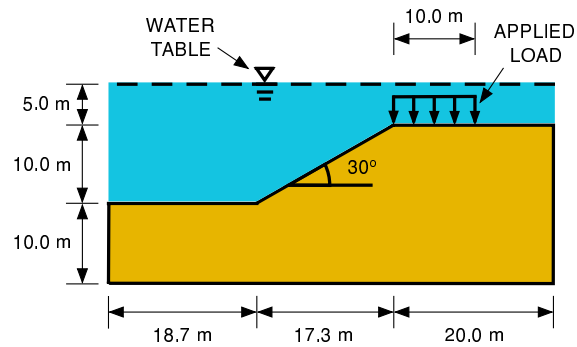


Figure 4: Dimensions and loading conditions for Case 3: Submarine slope.

Accepted Manuscript
Not Copyedited

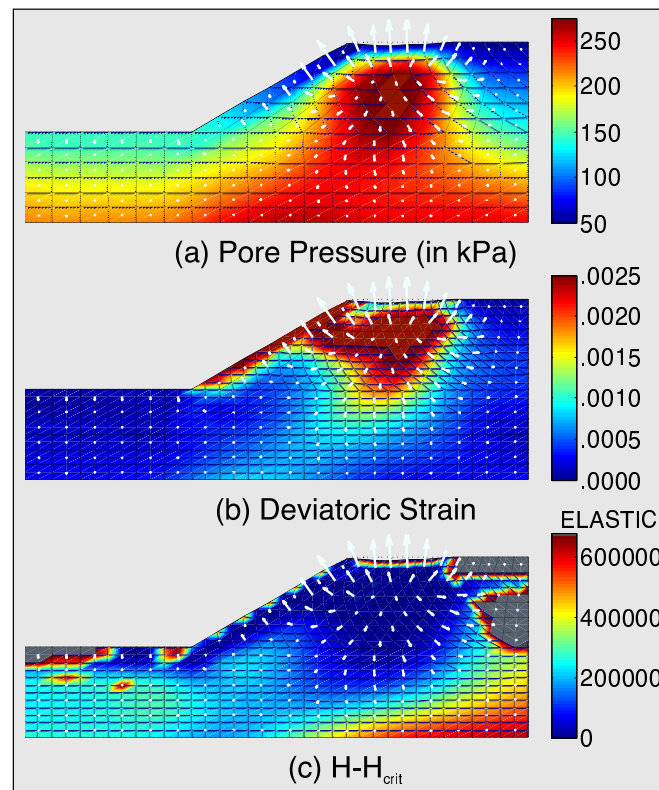


Figure 5: Map of pore pressure, deviatoric strain and $H - H_{crit}$ at failure for Case 3: Submarine slope. (Note: Deformations are magnified $\times 10$).

Accepted Manuscript
Not Copyedited

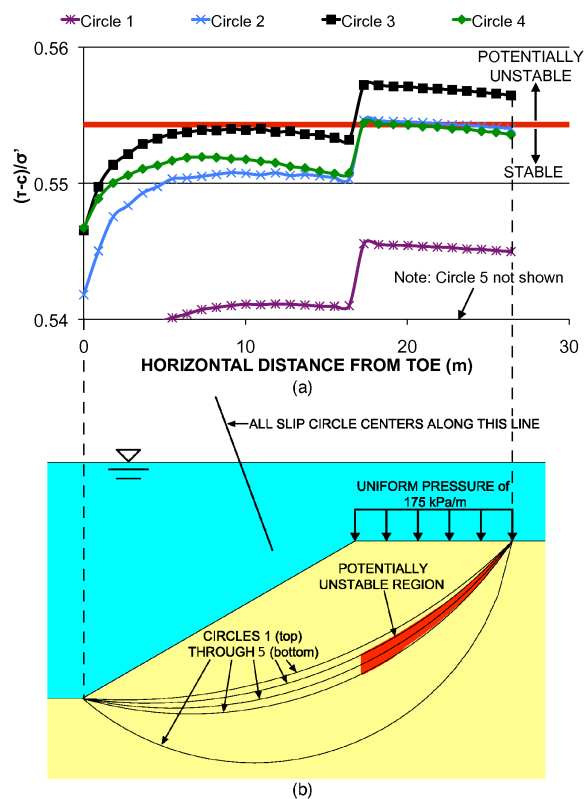


Figure 6: Mapping of potentially unstable region using method from Lade [1992].

Accepted Manuscript
Not Copyedited

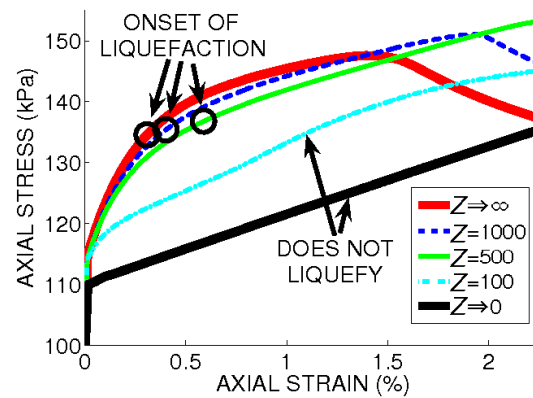


Figure 7: Drained plane strain compression predictions at various loading rates.

Accepted Manuscript
Not Copyedited

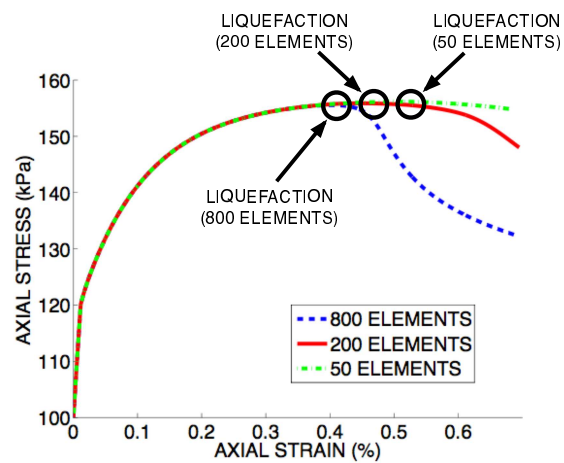


Figure 8: Undrained plane strain compression predictions for 50, 200 and 800 element mesh sizes.

Accepted Manuscript
Not Copyedited

	Plane Strain Tests		Submarine Slope
	Case 1	Case 2	
Side B.C.'s	$\sigma_x = -100$ kPa No Flow	$\sigma_x = -100$ kPa No Flow	$u_x = 0$ No Flow
Bottom B.C.'s	$u_y = 0$ No Flow	$u_y = 0$ $p = 0$	$u_y = 0$ No Flow
Top B.C.'s	$\sigma_y = -100$ kPa No Flow	$\sigma_y = -100$ kPa $p = 0$	$\sigma_y = -\gamma_f h$ $p = \gamma_f h$
Shearing Mechanism	Decrease u_y along top	Increase p along bottom	Decrease σ_y near top of slope

Table 1: Summary of initial boundary conditions (B.C.'s) and shearing mechanisms

Accepted Manuscript
Not Copyedited

Case	M	μ_0 (kPa)	$\hat{\kappa}$	$\hat{\lambda}$	v_{c0}	h	N	\bar{N}	ρ
1 to 2 (PS Tests)	1.20	45,000	0.005	0.020	1.80	70	0.4	0.2	0.78
3 (Submarine Slope)	1.27	45,000	0.0015	0.020	1.89	70	0.4	0.2	0.78

Table 1: Summary of constitutive model parameters

Accepted Manuscript
 Not Copyedited